

An Eulerian diffuse-interface method for simulation of elastic capsules in flow

Kiran Satheeshchandran¹, Salar Zamani Salimi², Lisa Prahl Wittberg¹, and Luca Brandt³

¹*FLOW, Department of Engineering Mechanics, KTH, 10044 Stockholm, Sweden*

²*Department of Energy and Process Engineering, Norwegian University of Science and Technology (NTNU), 7491 Trondheim, Norway*

³*Department of Environment, Land and Infrastructure Engineering (DIATI), Politecnico di Torino, 10129 Turin, Italy*

Abstract

Elastic interfaces with varying levels of permeability are widely encountered in nature. Red blood cells, for example, are characterized by an area-incompressible membrane that is permeable to the diffusion of oxygen and carbon dioxide. Artificial capsules, on the other hand, are often engineered to remain impermeable until they reach a designated location or time, whereby they release their internal contents into the surrounding medium. A common approach to numerical simulations of elastic capsules in flow involves discretizing the membrane surface to facilitate the calculation of shear strains and area changes. Recently, level-set-based methods that rely on advection of the reference map between the deformed and reference configurations have proven to be a promising alternative. This approach offers several advantages, including ease of implementation and parallelization. In the present work, we adapt the levelset based formulation to a diffuse interface framework to overcome the intrinsic limitation of the level set to conserve mass. We show that by adding a variational term to the reference map advection equation, consistency between the interface location (defined using a reference map) and the diffused interface can be ensured. Through a number of validation cases, we show the accuracy and robustness of the present approach. In addition, we extend the framework to multi-capsule simulations, demonstrating the ability of handling hundreds of discrete capsules with minimal additional computational cost.

1 Introduction

Liquid-filled capsules are commonly encountered in both natural and biological flows, and play a critical role in a variety of industrial applications—particularly in the pharmaceutical

sector, where they are widely employed as drug carriers or delivery agents. These capsules are often transported by a carrier fluid—such as water or blood plasma—to a targeted region of the body to release their internal contents. Computational modeling has been widely used recently to better understand and optimize behavior of capsules in various flow environments. Vesicles and red blood cells (RBCs), sharing similar deformable membrane characteristics, are often modeled using the same numerical frameworks to study their transport through capillary networks in the body.

Numerical simulations of capsules in complex flow environments typically involve three primary components: (1) solving the governing equations for the carrier fluid to compute the velocity and pressure fields, (2) evaluating membrane mechanics, including shear and bending forces, and (3) coupling of the fluid and membrane dynamics. Ramanujan and Pozrikidis [1] employed the boundary element method with a triangular surface discretization to investigate large deformations of capsules and the effects of internal-to-external viscosity ratios in the Stokes flow regime. Building on this, Doddi and Bagchi [2] and Li and Sarkar [3] extended the analysis to finite Reynolds number flows by coupling the front-tracking technique with finite-difference Navier–Stokes solver. Zhao et al.[4] developed a spectral boundary integral method to simulate the three-dimensional motion of biconcave RBCs through geometrically complex microfluidic domains. Fedosov et al.[5] adopted a multiscale modeling approach based on dissipative particle dynamics, capturing the RBC deformation dynamics in close agreement with experimental data. A comprehensive overview of relevant numerical approaches for modeling capsules, vesicles, and RBCs can be found in the book edited by Pozrikidis [6].

Almost all of the aforementioned methods rely on discretizing the membrane surface using a mesh of Lagrangian markers, where the connectivity between neighboring points must be preserved throughout the simulation. Maintaining this connectivity as the interface deforms and migrates introduces significant computational and implementation challenges. In distributed-memory flow solvers based on finite-difference or finite-volume methods, the computational domain is typically partitioned across processors. When a capsule moves across the processor boundaries, either the complete Lagrangian data structure must be communicated between processors, or global access to all interface data must be maintained on each processor. Both strategies introduce non-trivial complexity—either in terms of communication overhead or memory duplication—and become increasingly prohibitive in simulations involving large numbers of capsules or cells.

Recently, Milcent and Maître [7] proposed a fully Eulerian framework in which shear and area changes were computed directly from a backward reference map from the current state to the initial/reference configuration. By advecting a vector-valued reference map field alongside a level set function that tracks the interface, they demonstrated the relaxation of an initially sheared capsule immersed in a surrounding fluid solved by a finite-difference solver. The level set–based Eulerian formulations developed by Cottet, Maître, and Milcent for simulating soft solids, elastic membranes, and rigid bodies are comprehensively detailed in their monograph [8].

Building on the above works, Desmons et al.[9] simulated the passage of a nucleated capsule through a constriction using the fully Eulerian reference map formulation. More recently, Kloppe and Aland[10] introduced a phase field model capable of handling both elastic and viscoelastic interfaces in a fully Eulerian framework. While their method successfully captures shear forces in two-dimensional and axi-symmetric settings, they report significant challenges in extending the formulation to fully three-dimensional simulations.

Volume fraction based diffused interface methods are known to have better conservation properties compared to levelset methods. But such methods usually struggle to keep a sharp interface thickness in long time simulations resulting in difficulties in accurate interface force calculations. Recently, Conservative Diffuse Interface(CDI) methods based on phase field methods are shown to alleviate many of the drawbacks of the original formulations [11]. By including a regularization term in the advection equation, CDI methods are shown to keep the interface thickness fixed throughout the simulation while maintaining volume conservation. By adding corresponding terms in the momentum equation, such methods were also shown to be energy conserving [12]. The main advantage of such methods is the ease in implementation, parallel scalability and good conservation properties. A comparison of numerical methods for two phase flows could be found in the paper by Mirjalili et al. [13].

In the present work, we couple the membrane formulation proposed by Milcent and Maître [7] with a diffused interface framework to enable robust, long-time simulations of capsule dynamics. Specifically, we employ a conservative diffuse interface method for the volume fraction advection, combined with a consistent advection of the reference map field achieved through a variational correction term. This Eulerian approach eliminates the need for explicit Lagrangian tracking, while maintaining the ability to capture large deformations and the long-time behavior of many capsules. In fact, we demonstrate that the reference map field itself can serve as a powerful tool for tagging and tracking individual capsules in multi capsule simulations, eliminating the need for global connectivity data structures or MPI communication. The effectiveness of the proposed framework is validated through a series of benchmark simulations involving both single and multiple capsules.

This paper is organized as follows. The governing equations for the fluid flow and the membrane model are presented in Section 2. Numerical methods used for solving the advection equation, the reference map evolution, and the fluid flow equations are described in Section 3, which also introduces the proposed tagging procedure for multi capsule simulations. Validation studies for both single and multiple capsules in various flow scenarios are presented in Section 4. Finally, the paper concludes with a summary and discussion in Section 5.

2 Mathematical Formulation

We consider two-phase flows with a thin impermeable elastic membrane separating the two phases. Both phases are considered Newtonian and are governed by the incompressible N-S equations

$$\nabla \cdot \mathbf{u} = 0, \quad (1)$$

$$\rho \left[\frac{\partial \mathbf{u}}{\partial t} + (\mathbf{u} \cdot \nabla) \mathbf{u} \right] = -\nabla p + \nabla \cdot [\mu (\nabla \mathbf{u} + \nabla \mathbf{u}^T)] + \mathbf{F}. \quad (2)$$

The source term \mathbf{F} is the membrane force that is local to the interface. We use a one-fluid formulation where density (ρ) and viscosity (μ) are represented as functions of an indicator function, ϕ , as below,

$$\rho = \phi \rho_1 + (1 - \phi) \rho_2, \quad (3)$$

$$\mu = \phi \mu_1 + (1 - \phi) \mu_2, \quad (4)$$

where the subscript 1 is used for the dispersed phase and 2 is used for the carrier phase. In the present work, we use the volume fraction as the indicator function that changes from one inside the interface to zero outside.

We follow the work of Milcent et al. [7] to compute the membrane force \mathbf{F} . To this end, let us introduce the reference map ζ at (\mathbf{x}, t) from the current configuration to the reference configuration at (\mathbf{X}, t_0) ; the deformation gradient tensor and the left Cauchy-Green Tensor are then computed using the reference map ζ as

$$\mathcal{F} = [\nabla_x \zeta]^{-1}, \quad \mathcal{B} = \mathcal{F} \mathcal{F}^T. \quad (5)$$

We also define a modified tensor \mathcal{P} that projects \mathcal{B} onto the tangential plane to the interface:

$$\mathcal{P} = \mathcal{B} - \frac{(\mathcal{B} \mathbf{n}) \otimes (\mathcal{B} \mathbf{n})}{(\mathcal{B} \mathbf{n}) \cdot \mathbf{n}}, \quad (6)$$

where \mathbf{n} is the unit normal to the interface.

The membrane force is computed from an elastic energy as

$$\mathbf{F} = \nabla \cdot \left[\frac{\partial W}{\partial \eta_1} \eta_1 (\mathbf{I} - \mathbf{n} \mathbf{n}) + \frac{\partial W}{\partial \eta_2} \eta_2 \left(\frac{2\mathcal{P}}{\text{Tr}(\mathcal{P})} - (\mathbf{I} - \mathbf{n} \mathbf{n}) \right) \right] \delta_\epsilon(\psi), \quad (7)$$

where W is the strain energy obtained from a constitutive law and \mathbf{I} is the identity tensor. The coefficients η_1 and η_2 are the measures that quantify the area change and shear on the membrane surface, respectively; these are defined from the nonzero eigenvalues λ_1^2 and λ_2^2 of \mathcal{P} as

$$\eta_1 = |\lambda_1 \lambda_2|, \quad (8)$$

$$\eta_2 = \frac{1}{2} \left(\left| \frac{\lambda_1}{\lambda_2} \right| + \left| \frac{\lambda_2}{\lambda_1} \right| \right). \quad (9)$$

In the expression (7), $\delta_\epsilon(\psi)$ denotes a numerical Dirac delta to localize the forces to the interface, which is introduced in the next section. Without any loss of generality, we restrict the present study to Neo-Hookean capsules with the constitutive law given as

$$\frac{\partial W}{\partial \eta_1} = G_s(\eta_2 - \frac{1}{\eta_1^3}), \quad \frac{\partial W}{\partial \eta_2} = G_s \eta_1; \quad (10)$$

where G_s is the membrane shear stiffness.

3 Numerical Implementation

3.1 Interface advection

The accurate advection of the volume fraction field in the diffuse interface framework has been challenging due to the difficulty in maintaining the interface thickness constant in long-time simulations, often resulting in volume losses for the dispersed phase. The Conservative Diffuse Interface (CDI) formulation [11, 14] has shown significant promise in addressing many of the shortcomings of the previous methods in this regard. In the CDI method, ϕ is advected by

$$\frac{\partial \phi}{\partial t} + \nabla \cdot (\mathbf{u}\phi) = \nabla \cdot \left[\gamma \left(\alpha \nabla \phi - \phi(1-\phi) \frac{\nabla \phi}{|\nabla \phi|} \right) \right] \quad (11)$$

where the right-hand side is a regularization term that keeps the interface sharp. The parameter γ is a velocity scale and α a length scale defining the interface thickness. We keep $\frac{\gamma}{|\mathbf{u}|_{max}} = 1$, where $|\mathbf{u}|_{max}$ is the magnitude of the maximum velocity in the simulation, and $\alpha = 1$ in all our simulations. We use a second order central scheme for discretizing the advection term and the RK3 scheme for time marching.

The interface normal is computed from the gradient of the volume fraction field [15] as

$$\mathbf{n} = \frac{\nabla \phi}{|\nabla \phi|}. \quad (12)$$

We also construct an approximate signed distance field ψ from ϕ [12] as

$$\psi = \alpha \ln \left(\frac{\phi + \varepsilon}{1 - \phi + \varepsilon} \right). \quad (13)$$

Here ε is a very small number that avoids division by zero. Note that the iso-contour $\phi = 0.5$ corresponds to $\psi = 0$. We make use of this levelset function in many of the algorithms in the present work with $\psi > 0$ indicating regions inside the interface while $\psi < 0$ identify regions outside the interface.

We use the levelset field to define the numerical Dirac delta function as $\delta_\epsilon(\psi)$

$$\delta_\epsilon(\psi) = \begin{cases} \frac{1}{2\epsilon} \cos(1 + \frac{\psi}{\epsilon}), & \text{if } |\psi| \leq \epsilon \\ 0, & \text{otherwise} \end{cases} \quad (14)$$

with ϵ an interface thickness parameter which is set to $1.5\Delta x$ where Δx is the grid spacing.

3.2 Consistent transport of the reference map

To calculate the membrane strain at any given time, as defined in Equation 5, it is necessary to know the reference map at each grid point on the interface at any instant of time. This is achieved by advecting the reference map field $\zeta(\vec{x}, t)$ from a given initial configuration. Typically, this can be done as $\zeta(\vec{x}, 0) = \vec{x} = \vec{X}$, where \vec{X} denotes the initial material coordinate. This initialization is appropriate in the absence of pre-strain. For problems involving pre-strained membranes, ζ can be initialized to reflect the known initial deformation, as discussed by Desmons et al. [9].

Each component of the reference map is advected using the following transport equation

$$\frac{\partial \zeta_i}{\partial t} + (\mathbf{u} \cdot \nabla) \zeta_i = 0 \quad (15)$$

where \mathbf{u}_i denotes the fluid velocity field on the background Eulerian mesh. Numerically, this equation is discretized in space using a fifth-order WENO (WENO5) scheme and advanced in time using a third-order Runge–Kutta scheme.

With this reference map approach, the interface can be defined in two ways:

- As the zero of the level set field $\psi(\vec{x}, t)$, obtained from the phase field function (see eq. 13):

$$\psi(\vec{x}, t) = 0. \quad (16)$$

- As the zero of the initial level set function evaluated at the mapped coordinates from the reference map, $\Psi(\vec{x}, t) = \psi(\zeta(\vec{x}, t), 0)$:

$$\Psi(\vec{x}, t) = 0. \quad (17)$$

Physically, the interface captured by the level set function $\psi(\vec{x}, t) = 0$ represents the actual fluid–membrane–fluid boundary during the simulation. In contrast, the reference-map-based interface defined by $\Psi(\vec{x}, t) = 0$ tracks the material origin of interface points from the initial configuration. Ideally, these two interfaces should remain coincident throughout the simulation. However, due to differences in the numerical advection schemes and the accumulation of discretization errors, a gradual drift between them is observed, manifesting as discrepancies in the zero contours of the two level set functions.

To illustrate this behavior, we consider the case of a spherical capsule subjected to a simple shear flow (see Section 4.1 for the simulation details). Figure 1a shows the location of the interface obtained with the two definitions above, after the capsule reaches its equilibrium shape. The mismatch between the two is evident, particularly near the extremities of the deformed capsule, where the curvature is the highest. This discrepancy can negatively affect the stress computation and thereby distort the predicted capsule shapes.

To maintain consistency in their simulation of soft solids in flow with a levelset-based interface advection Valkov et al. [16] imposed the condition that both interfaces match exactly:

$$\Psi(\vec{x}, t) = 0 \iff \psi(\vec{x}, t) = 0. \quad (18)$$

In practice, this condition is often enforced by redefining the levelset field from the reference map at every timestep, followed by a re-initialization step to preserve its signed-distance property.

However, in the present diffuse-interface formulation, ψ is derived from the volume fraction field ϕ , and such direct reconstruction is not feasible. Instead, we adopt a variational approach to maintain consistency between the reference map and the diffused interface location. Variational methods have previously been employed in level set advection [17] to avoid explicit re-initialization by continuously enforcing interface properties.

We therefore define an error functional that quantifies the discrepancy between the two interface definitions—the diffused interface $\psi(\vec{x}, t)$ and the reference map–based interface $\Psi(\vec{x}, t)$ —as follows:

$$E = \int_{\Omega} (\Psi - \psi)^2 \delta_{\epsilon}(\psi) d\Omega. \quad (19)$$

Here, the smoothed Dirac delta function $\delta_{\epsilon}(\psi)$ defined in the previous section (see eq. 14) restricts the error evaluation to a narrow region surrounding the interface. To minimize this error and thereby drive the reference map–based interface toward the diffused interface, we introduce a source term into the reference map advection equation:

$$\frac{\partial \zeta_i}{\partial t} + (\mathbf{u} \cdot \nabla) \zeta_i = -\frac{\delta E}{\delta \zeta_i}. \quad (20)$$

Taking the functional derivative of E with respect to ζ_i , we have:

$$\frac{\delta E}{\delta \zeta_i} = 2(\Psi - \psi) \frac{\partial \Psi}{\partial \zeta_i} \delta_{\epsilon}(\psi). \quad (21)$$

Next, from the definition of $\Psi(\vec{x}, t)$, we can write:

$$\frac{\partial \Psi}{\partial \zeta_i} = \frac{\partial \psi(\vec{\zeta}, 0)}{\partial \zeta_i}, \quad (22)$$

where $\frac{\partial \psi(\vec{\zeta}, 0)}{\partial \zeta_i}$ denotes how the initial levelset field changes with respect to perturbations in the reference map. If $\psi(\vec{\zeta}, 0)$ is known analytically or numerically from the initial configuration, which is usually the case in all the simulations, $\frac{\partial \psi}{\partial \zeta_i}$ can be explicitly computed.

Thus, the forcing term in the advection equation for the reference map becomes

$$\frac{\delta E}{\delta \zeta_i} = 2(\Psi - \psi) \frac{\partial \psi(\vec{\zeta}, 0)}{\partial \zeta_i} \delta_{\epsilon}(\psi). \quad (23)$$

Substituting this into the advection equation, we finally obtain

$$\frac{\partial \zeta_i}{\partial t} + (\mathbf{u} \cdot \nabla) \zeta_i = -2(\Psi - \psi) \frac{\partial \psi(\vec{\zeta}, 0)}{\partial \zeta_i} \delta_{\epsilon}(\psi). \quad (24)$$

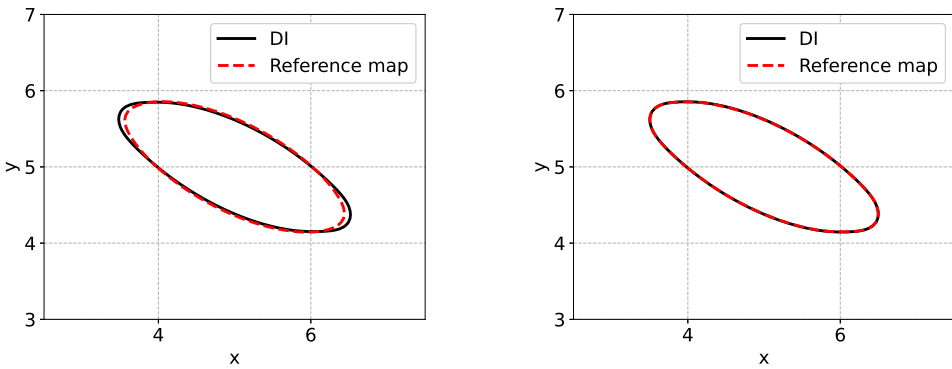


Figure 1: a) Definition of the interface from the diffused interface (solid) and the reference map (dotted) after (a) inconsistent transport and b) after introducing the variational term described in the text to enforce a consistent transport [Ca=0.6, $t^* = 2$]

The modified advection equation provides a way to advect the reference map consistently with the evolution of the diffused interface over long-time simulations. To illustrate this, we have performed the same simulation of spherical capsule in shear flow with the addition of the variational term. Figure 1b shows that the consistent transport of the two functions leads to the interfaces overlaying over each other after the same simulation time.

3.3 Extrapolation and filtering of the reference map

During the advection of the reference map, the values of ζ at grid points away from the interface can differ significantly from those near the interface, particularly in regions experiencing large velocity gradients. This can lead to artificially large computed strains, resulting in unphysically large stresses and potentially causing divergence in the flow solver. To avoid this issue, simulations involving fluid–soft solid interactions typically employ an extrapolation of the reference map values from the solid region into the surrounding fluid region [18]. Such extrapolation ensures bounded strain calculations away from the interface. Commonly used extrapolation techniques include PDE-based methods such as Aslam extrapolation, as well as least-squares–based methods [19].

For closed elastic membranes interacting with fluid on both sides—inside and outside—the reference map must be updated outwards from the interface in both directions. Desmons et al. [9] demonstrated that performing an Aslam extrapolation outside the interface and a diffusion step within the capsule region (termed ‘inner diffusion’) is sufficient to maintain accurate strain calculations.

In this work, we use Aslam extrapolation to propagate the reference map outwards, employing a first-order upwind scheme for the spatial discretization, combined with a first-order explicit time stepping. To mitigate the numerical oscillations resulting from the extrapolation, we perform a filtering operation on cells located outside the capsule region

(where the levelset satisfies $\psi < 0$), following the procedure outlined by Valkov et al. [16]. The algorithms are summarized below.

In all simulations presented here, we first perform one iteration of inner diffusion within the capsule region ($\psi > 0$) using a CFL number of 0.1. Following this, we execute 20 iterations of Aslam extrapolation with a CFL number of 0.2. After extrapolation, a single filtering step is carried out with a CFL number of 0.05. Note that these additional numerical procedures also introduce unwanted errors into the solution and are computationally expensive. Hence we carry out these operations only as frequent as the problem demands. A detailed sensitivity study of the above parameters on the solution can be found in section 5.4.

3.4 Tagging using the reference map for multi capsule simulations

Many physical problems of practical interest involve simulations with multiple capsules or blood cells, thus requiring the extension of our current computational framework to handle multi-capsule scenarios. Unlike traditional front-tracking methods, where computational complexity scales almost linearly with the number of discrete capsules due to the increasing numbers of Lagrangian markers, the reference map method efficiently represents multiple capsules within a single vector field. This approach provides substantial advantages in data management, memory efficiency, and parallel scalability.

Since the consistent variational advection scheme described in the previous section is explicitly based on each capsule's unique reference configuration, multicapsule simulations require an effective capsule-tagging procedure at each time step. We demonstrate that capsule identification and tagging can be efficiently implemented using the reference map field itself. The proposed tagging method avoids costly MPI communication and by employing hash tables for spatial search, significantly reduce the computational overhead.

Spatial hashing has been widely used in numerical simulations for neighbor detection and collision modeling [20, 21]. We briefly describe the spatial hash algorithm we implement to efficiently search the capsule reference maps. The key steps during hash table initialization and the assignment of capsules to each hash bin are presented in Algorithm 1. For ease of explanation, we assume that capsules are initially spherical; however, the algorithm is general and valid for other shapes (e.g., ellipsoidal or biconcave), as long as an analytical formula for the reference geometry is available.

We begin by computing a global bounding box—a rectangular subregion of the domain enclosing all capsules. A buffer factor β defines an extended region around each capsule so that nearby grid points can be included in tagging if needed. In our simulations, we use $\beta = 1.25$, although this can be adjusted depending on the volume fraction or initial capsule distribution.

The size of the bin is set using the average radius of the capsule, scaled by a factor ω . We use $\omega = 2.5$ in this work. A larger ω increases the number of capsules per bin, while a smaller value may cause individual capsules to span too many bins. Once the bin dimensions

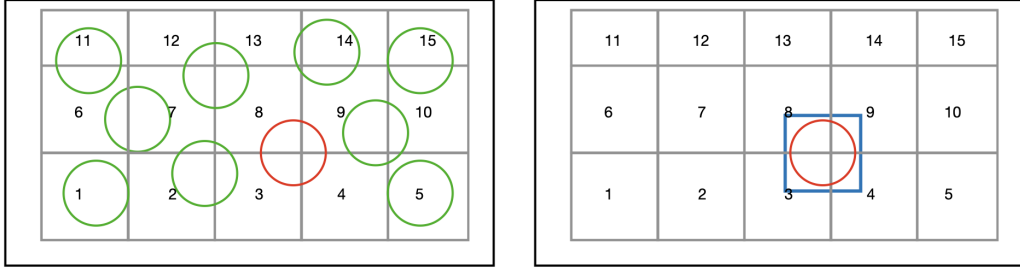


Figure 2: Global bounding box and bins in hash table for an arbitrary initial arrangement of spherical capsules (left). The simulation domain is given by the bigger outer box. Identification of hash bins for a capsule by construction of a local bounding box is shown on the right. See the corresponding Algorithm. 1.

are established, each bin is populated with all capsules that spatially overlap it. A schematic of the above steps is shown in Figure 2.

After the hash table initialization, tagging of the grid points is performed using the reference map field. For each grid point, we reconstruct the signed distance function in the reference configuration using the capsule-shape analytical formula. For instance, for a spherical capsule:

$$\Psi(\mathbf{x}, t)_d = r_d - \sqrt{(\zeta_x - c_x)^2 + (\zeta_y - c_y)^2 + (\zeta_z - c_z)^2}, \quad (25)$$

where Ψ_d is the signed distance from the capsule valid in the neighborhood of capsule "d" and c is the location of the center of the capsule at $t = 0$. If $\Psi_d > 0$, the grid point is within capsule d, and its tag is set accordingly.

It is important to finally note that, since the hash table is replicated on each processor and the tagging is performed locally, no inter-process communication (MPI) is required.

3.5 Flow solver

The membrane dynamics and reference map advection algorithms detailed in the preceding sections must be coupled to a Navier–Stokes (N–S) solver, which provides the instantaneous velocity field at each timestep. In the present work, we utilize the open-source solver CaNS, which employs a highly efficient and scalable FFT-based method for solving the pressure Poisson equations [22]. This numerical choice currently restricts the validation simulations presented here to fluids with matched density and viscosity (density and viscosity ratio of unity between inner and outer fluids). However, we emphasize that the proposed computational framework itself imposes no intrinsic limitations on fluid density or viscosity ratios and can be straightforwardly coupled to other existing multiphase solvers (see for eg. [15]).

CaNS solves the incompressible Navier–Stokes equations on structured Cartesian grids using a fractional-step pressure correction scheme. The spatial discretization of the momentum

Algorithm 1 Hash table initialization and assignment of capsules to hash bin

```
1: procedure INITHASHTABLE
2:   for all capsules  $d$  do
3:     Compute bounding box:

$$\mathbf{x}_{\min} \leftarrow \min(\mathbf{x}_{\min}, \mathbf{c}_d - \beta r_d)$$


$$\mathbf{x}_{\max} \leftarrow \max(\mathbf{x}_{\max}, \mathbf{c}_d + \beta r_d)$$

4:   end for
5:   Estimate average capsule radius  $\bar{r}$ 
6:   Set bin size:  $\Delta x_{\text{bin}} \leftarrow \omega \cdot \bar{r}$ 
7:   Compute number of bins:

$$n_i \leftarrow \left\lceil \frac{x_{\max}^{(i)} - x_{\min}^{(i)}}{\Delta x_{\text{bin}}} \right\rceil \quad \text{for } i = 1, 2, 3$$

8:   for all capsules  $d$  do
9:     Determine bounding box of capsule  $d$  using  $r_d$ 
10:    Compute index range of bins overlapped by this bounding box
11:    for all bins within this index range do
12:      Append capsule ID  $d$  to the corresponding hash bin
13:    end for
14:   end for
15: end procedure
```

Algorithm 2 Tagging grid points using reference map and hash search

```
1: procedure ASSIGNCAPSULETAGS
2:   for all grid points  $\mathbf{x}$  do
3:     Determine hash bin corresponding to  $\zeta(\mathbf{x})$ 
4:     for all Capsules  $d$  in that bin do
5:       Compute  $\Psi_d$ 
6:       if  $\Psi_d > 0$  then
7:         Assign tag  $\leftarrow d$ 
8:         break inner loop
9:       end if
10:      end for
11:    end for
12: end procedure
```

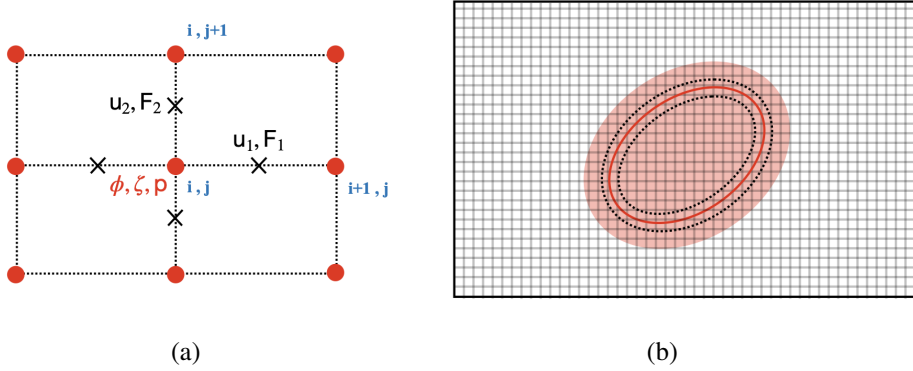


Figure 3: a) Staggered grid arrangement for the solver. b) Schematic of a typical simulation configuration. The interface is shown as black solid line while the part of the domain where the reference map is advected is shown in color. The membrane force computation is carried out only inside the region around the interface delimited by dotted lines.

equations is carried out using second-order finite differences, while the temporal discretization employs a third-order Runge–Kutta (RK3) scheme. In our simulations, the advection terms are treated explicitly, while the viscous terms are discretized implicitly to enable larger time steps, particularly beneficial in low-Reynolds-number simulations. The implicit discretization leads to Helmholtz-type equations in each spatial direction, which are efficiently solved using FFT-based solvers [23]. Figure 3a shows the staggered arrangement of variables in the solver. Below, we briefly describe the coupling strategy between the flow solver and the membrane-advection algorithms.

After initializing all fields, we begin each time step by tagging individual capsules using the algorithm described in the previous section. This is followed by the advection of the phase field ϕ , and subsequently, the advection of the reference map field ζ . Once ζ is updated, the membrane forces corresponding to the next partial time step are computed, after which the Navier–Stokes equations are solved. These steps—from field advection to force evaluation and the solution of the fluid momentum equation, are carried out at each sub-step of the three-stage Runge–Kutta (RK) scheme. At the end of each full RK step, additional operations such as inner diffusion, Aslam extrapolation, and filtering are performed, depending on the prescribed frequency. This sequence of operations is repeated at every time step until the end of the simulation.

Since the reference map field is frequently extrapolated from the interface, we could restrict the advection of ζ to the regions close to the interface in the carrier phase. Figure 3a shows a schematic of the different relevant regions where the various calculations are performed. The black curve shows the interface location with the shaded region indicating the region inside which the indicator functions are advected. The curves on either side of the interface indicate where the membrane force calculation is active. We maintain an active

advection region of 10 cells outside the interface and restrict the force calculation to 4 cells on either side of the interface for the results in the present work.

4 Validation

We now present a series of validation cases that demonstrate the capability of the proposed framework across simulations of increasing complexity. We begin with the classical case of a spherical capsule in shear flow, a standard benchmark for assessing membrane–fluid interaction models. After describing the simulation setup and presenting the grid convergence results, we examine the effect of the membrane shear stiffness on the capsule’s deformation and inclination angle.

Next, we simulate a capsule traversing a rectangular channel to validate the method’s robustness in internal flow configurations. This is followed by a two-capsule shear flow simulation used to verify the accuracy of the tagging algorithm for identifying and tracking individual capsules. Finally, we perform large-scale simulations of many capsules in a channel flow to demonstrate the framework’s ability to efficiently handle realistic, many-body capsule dynamics.

4.1 Spherical capsule in shear flow

A spherical capsule of diameter R is placed in the center of a rectangular domain of size $10R \times 10R \times 5R$ in the x, y and z directions, respectively. Linear shear flow is imposed on the capsule along the x direction, $U(y)$. The periodic boundary condition is set in the x and z directions while the no-slip boundary condition is set in the y direction. The deformation of the capsule is characterized by the Taylor deformation parameter, defined as $(D_{xy}) = \frac{a-b}{a+b}$,



Figure 4: Flow chart showing the overall algorithm ability to efficiently handle realistic, coupling the flow solver and the membrane calculations many-body capsule dynamics.

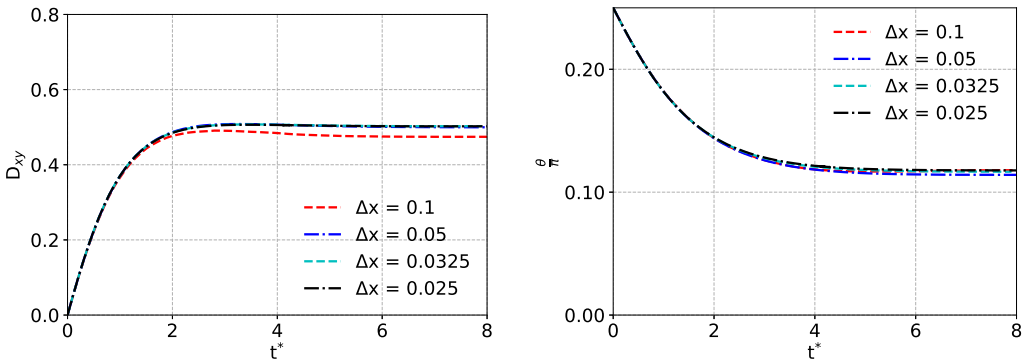


Figure 5: Grid Convergence of a) Taylor deformation parameter D_{xy} and b) angle of inclination θ versus the non-dimensional time for a spherical capsule in shear flow at Reynolds number of 0.1 and Capillary number of 0.6

where a and b are the major and minor axis (in the xy plane) of an ellipsoid with the same moment of inertia as the capsule. The inclination of the capsule major axis with respect to the flow direction x is given by θ .

The Reynolds number $Re = \frac{\rho \dot{\gamma} R^2}{\mu} = 0.1$ to match closely with the reference intertialess cases reported in the literature (see, e.g. [3]). The Capillary number ($Ca = \frac{\mu \dot{\gamma} R}{G_s}$) is varied from 0.075-0.9 by varying the membrane stiffness, G_s .

4.1.1 Grid Convergence

To check the grid convergence of the solution for capsule deformations, we choose the value of the capillary number $Ca = 0.6$ as the capsule deformation is comparatively high for this case than for stiffer capsules. We change the resolution of the grid progressively from $\Delta x = 0.1$ to $\Delta x = 0.025$. A fixed time step of $\Delta t = 5.0e-4$ is kept for all simulations. The extrapolation and diffusion steps are carried out once every 20 N-S iterations. From figure 5, we can see that the simulation has converged at a resolution of $\Delta x = 0.03125$ that corresponds to $320 \times 320 \times 160$ grid cells. We use this grid resolution in our next study on the effect of Capillary number on the capsule deformation.

4.1.2 Effect of Capillary number

Next, we look at the effect of the stiffness of the capsule membrane on the deformation and inclination angle by varying the Capillary number from $Ca = 0.075$ to $Ca = 0.9$. Figure 6 displays the time evolution of the capsule deformation and inclination angle from the initial transient to the final equilibrium shape. Note that the simulation continues for long non-dimensional times in the equilibrium position, showing the robustness of the present numerical approach.

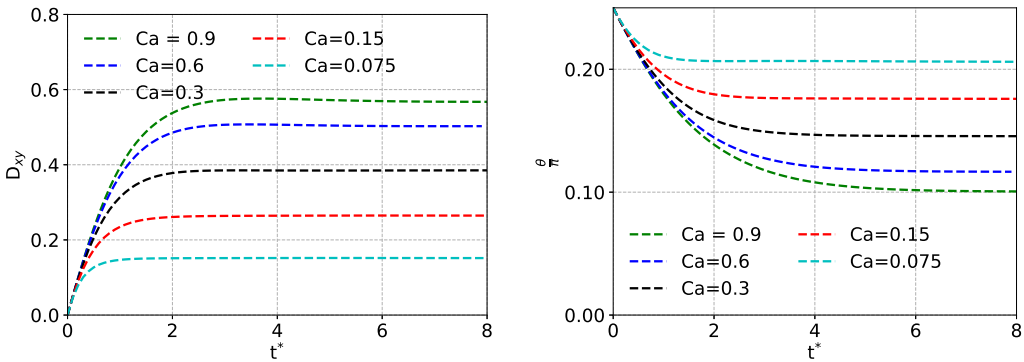


Figure 6: Evolution of a) the Taylor deformation parameter D_{xy} and b) the angle of inclination θ versus non-dimensional time for various Capillary numbers for the case of a spherical capsule in shear flow

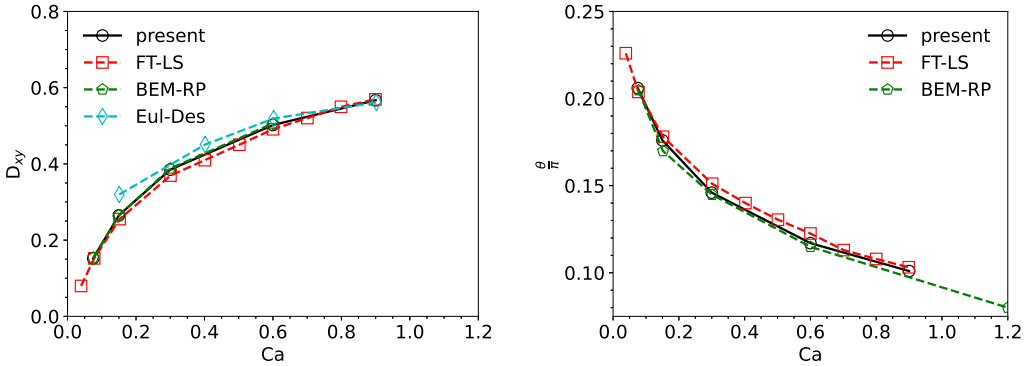


Figure 7: Variation of a) the Taylor deformation parameter D_{xy} and b) the angle of inclination θ with the Capillary number for a spherical capsule in shear flow compared against the reference results of Li and Sarkar(FT-LS [3]), Ramanujan and Pozrikidis(BEM-RP [1]) and Desmons et al.(Eul-Des [9]).

In order to further demonstrate the accuracy of the present approach, we compare our results with previous results reported in the literature and obtained with other numerical methods. As can be seen in figure 7, our results closely match the results of Li and Sarkar [3] who adopted a front tracking-finite difference scheme and with those of Ramanujan and Pozrikidis [1] using a boundary element method (BEM). In Figure 7a, we also show the values of the Taylor parameter for the capsule deformation obtained by Desmons et al. [9] using their fully Eulerian implementation.

4.1.3 Sensitivity of the numerical solution to Aslam extrapolation and inner diffusion

As discussed earlier in Section 3.3, it is important to perform Aslam extrapolation and inner diffusion at an optimal frequency relative to the Navier–Stokes iterations. While applying

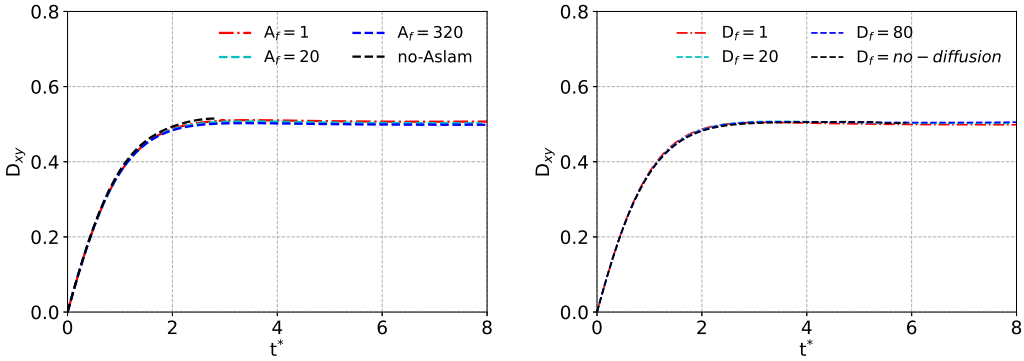


Figure 8: Sensitivity of the Taylor deformation parameter D_{xy} to the frequency of the Aslam extrapolation (left) and Inner diffusion (right) for the case of a spherical capsule in shear flow at $Ca=0.6$. The values in the legend refer to the number of steps of the Navier-Stokes solver before the next extrapolation/inner-diffusion operation is performed. **I woudl add a simbol, like a cross or a skull, a sign of death at the last instant before failure or crashing**

Aslam extrapolation at every flow time step is often desirable—and has been adopted in several previous studies on soft solids (see, e.g., [16])—it is computationally expensive and unnecessary in the low Reynolds number and moderate capillary number regime considered in the present work. Similarly, applying inner diffusion too frequently can lead to excessive smoothing of the reference map field in addition to increasing the computational cost. To strike a balance between accuracy and efficiency, we conduct a sensitivity analysis by varying the iteration frequency of both the extrapolation and diffusion steps.

The time evolution of the Taylor deformation parameter D_{xy} when varying the frequency of the extrapolation/inner-diffusion operation is reported in figure 8. The data in the figure confirm the need to perform these extra operations for the simulations to converge. When this is the case, the relative errors appear as reasonable also with few extrapolation/diffusion steps. **I woudl add a simbol, like a cross or a skull, a sign of death at the last instant before failure or crashing**

Specifically, to quantify the sensitivity of the solution to the frequency of Aslam extrapolation, we fix the inner diffusion frequency to once every 20 Navier–Stokes time steps. The simulation parameters are identical to those used in the previous section, with a capillary number (Ca) of 0.6. The extrapolation frequency is systematically varied, starting from a baseline case where extrapolation is performed every flow time step, and then progressively reduced to once every 5, 10, 20, 40, 80, and 320 time steps, respectively. To test the limit scenario, we also perform a simulation with no extrapolation applied at all. This case diverges at time $t^* = 2.88$, highlighting the necessity of periodic extrapolation to keep the strain field well-behaved and the stress calculations bounded. The Taylor deformation parameter, measured once the capsule reaches its equilibrium shape, is reported for each case in Table 1.

Extrapolation frequency (A_f)	D_{xy}	Diffusion frequency (D_f)	D_{xy}
1	0.507	1	0.498
5	0.506	5	0.499
10	0.505	10	0.501
20	0.503	20	0.503
40	0.501	40	0.505
80	0.500	80	0.505
320	0.498	160	solution diverged at $t^* = 7.6$
no extrapolation	solution diverged at $t^* = 2.88$	no inner diffusion	solution diverged at $t^* = 5.95$

Table 1: Effect of Extrapolation and diffusion frequency on the Taylor Deformation Parameter D_{xy} at steady state($t^* = 8$).

To investigate the effect of inner diffusion on the solution stability and accuracy, we fix the Aslam extrapolation frequency to once every 20 Navier–Stokes time step and vary the inner-diffusion frequency across a range of values: 1, 5, 10, 20, 40, 80, and 160 time steps. The values of the deformation parameter D_{xy} at $t^* = 8$ are also summarised in Table 1. As above, we additionally consider the limit case in which no inner diffusion is applied. The simulation with a diffusion frequency of 160 diverges at $t^* = 7.6$, while the case with no diffusion diverges earlier at $t^* = 5.95$.

To conclude, we note that the final frequency we chose for the individual simulations is mentioned in each section along with other relevant parameters. Simulations within significantly different Reynolds and Capillary number regimes may require more frequent extrapolation and diffusion procedures.

4.2 Capsule in square channel

Next, we consider a spherical capsule of diameter D advected in a square channel. To reduce the elastic energy, the capsule eventually migrates to the duct center where it is advected at constant speed and shape. In our simulation, the boundaries along the streamwise direction x are set as periodic, and the lateral sides are treated as no-slip walls. The Reynolds number of the flow defined based on the mean velocity in the channel, U_m , and the width of the channel, l , $Re = \frac{\rho U_m l}{\mu}$ is kept constant at 0.1 for all simulations. The Capillary number, $Ca = \frac{\mu U_m}{G_s}$, is varied from 0.02 to 0.1. The confinement ratio $\frac{D}{l}$ is kept at 0.9.

All simulations are done with a grid size of $400 \times 200 \times 200$ in a domain of $2 \times 1 \times 1$ at a uniform resolution of 0.05. A constant time step of $5e-5$ is used with the Aslam extrapolation and inner diffusion carried out every 40 time steps for simulations of capsules with $Ca=0.1$

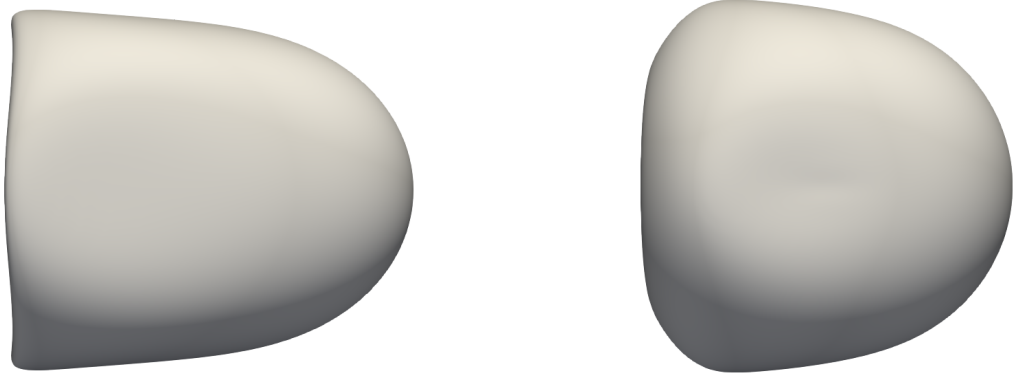


Figure 9: Steady state shape of a capsule advected in a square channel for $Ca = 0.1$ (left) and $Ca = 0.02$ (right).

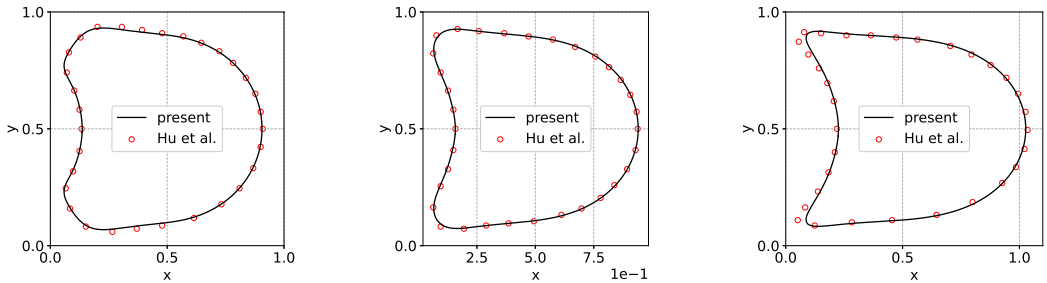


Figure 10: Comparison of the capsule shape in the wall-normal $x - y$ plane passing through the center of mass of the capsule for $Ca = 0.02$ (left), $Ca = 0.05$ (middle) and $Ca = 0.1$ (right). The reference results are from Hu et al. [24]

and $Ca = 0.05$. A small time step of $2.5e - 5$ is used for the case of a stiffer capsule with $Ca = 0.02$ with the extrapolation and diffusion still carried out every 40 time steps.

The steady-state three-dimensional shapes of the capsules for $Ca = 0.1$ and $Ca = 0.02$ are shown in Figure 9. The results of our simulations are compared with those reported by Hu et al. [24] that were obtained using a front tracking Finite element method for the membrane coupled with the Boundary Integral method for the fluid flow in figure 10 and 11. Specifically, we display the capsule shape in the xy plane for various Capillary numbers in figure 10, while figure 11 displays the shapes in the yz plane perpendicular to the flow direction. The results indicate the accuracy and robustness of the method in simulating capsules in internal channel flows for a wide range of Capillary numbers.

4.3 Hydrodynamic interaction of pair of capsules

We validate the multi-capsule algorithms introduced in section 3.4 by simulating a pair of spherical capsules interacting with each other in a shear flow. The setup is similar to that used for a single capsule in shear flow but with a larger domain of $30R \times 30R \times 5R$ to avoid wall effects on the capsule trajectories [25]. The Reynolds number is low enough ($Re = 0.01$)

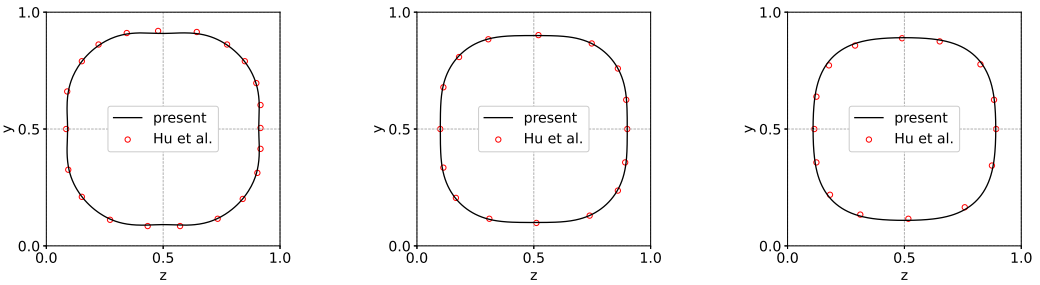


Figure 11: Comparison of the capsule shape in the cross-stream $x - y$ plane passing through the center of mass of the capsule for $Ca=0.02$ (left), $Ca=0.05$ (middle) and $Ca=0.1$ (right). The reference results are from Hu et al. [24]

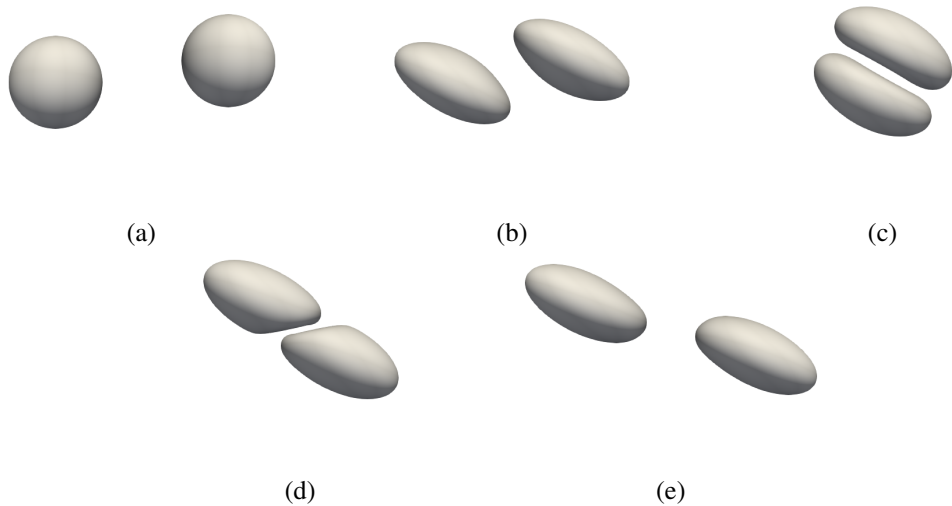


Figure 12: Capsule shapes for a pair of capsules at various instances of their interaction for initial centroid offset of $\Delta x = 4$, $\Delta y = 0.5$ and capillary number $Ca = 0.3$.

to avoid capsule overlap and collisions thanks to the lubrication pressure. In particular, we examine the effect of the initial offset of the capsule centroids and of the Capillary number on their interaction and subsequent trajectories. A uniform grid of size $960 \times 960 \times 160$ is used for all simulations with a time step of $2.5e-4$. Aslam extrapolation and diffusion are performed every 40 time steps.

Figure 12 displays the shapes of two capsules with $Ca = 0.3$ and initial offset of $\frac{\Delta x}{R} = 4$ and $\frac{\Delta y}{R} = 0.5$ at various instances during their interaction. The evolution of the two capsules is characterized by various phases such as 1) the initial deformation from the spherical shape to an ellipsoidal shape due to the effect of the underlying shear flow (see fig. 12b), 2) the capsule deformation and motion induced by the presence of the other capsule (see fig. 12c and fig. 12d) and 3) the recovery of the ellipsoidal shape once the capsules have moved away from each other (fig. 12e).

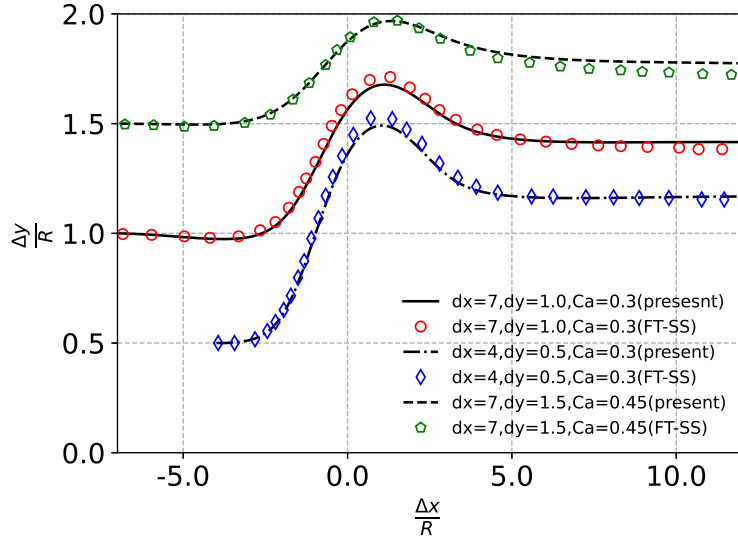


Figure 13: Comparison of the relative trajectory of the centroid of two capsules interacting with each other in a simple shear flow for different initial offsets and Capillary numbers. The reference data are from the simulations by Singh and Sarkar using the Front tracking method (FT-SS [25])

To quantitatively validate our implementation we consider classic results on capsule pair interactions. The time history of the relative offset between the capsule centroid is compared against the reference results from Singh and Sarkar [25] for three cases, a) $\Delta x = 4$, $\Delta y = 0.5$, $Ca = 0.3$, b) $\Delta x = 7$, $\Delta y = 1.0$, $Ca = 0.3$, c) $\Delta x = 7$, $\Delta y = 1.5$, $Ca = 0.45$, with the results shown in Figure 13. The excellent match confirms once more the ability of the proposed method to handle multi-capsule configurations even for cases where capsules are in close proximity.

4.4 Many-capsule simulations

One of the key advantages of a fully Eulerian framework for membrane and capsules (RBCs) modeling is its ability to simulate large numbers of capsules without a proportional increase of the computational cost, as highlighted earlier. To assess the scalability and efficiency of the proposed method, we conduct a series of simulations of elastic capsules suspended in a channel flow. The number of capsules N is systematically varied from 1 to 10, 50, 100, 200, and finally 500, while keeping the computational domain and all other simulation parameters fixed. The capsules are initially distributed randomly within the domain, with a minimum separation between capsules enforced to prevent overlap.

In particular, we consider a domain of size $20 \times 50 \times 20$ in units of capsule diameter in the x, y and z directions respectively. Periodic boundary conditions are imposed in the the y flow direction while the other two boundaries are treated as no-slip walls. We use a

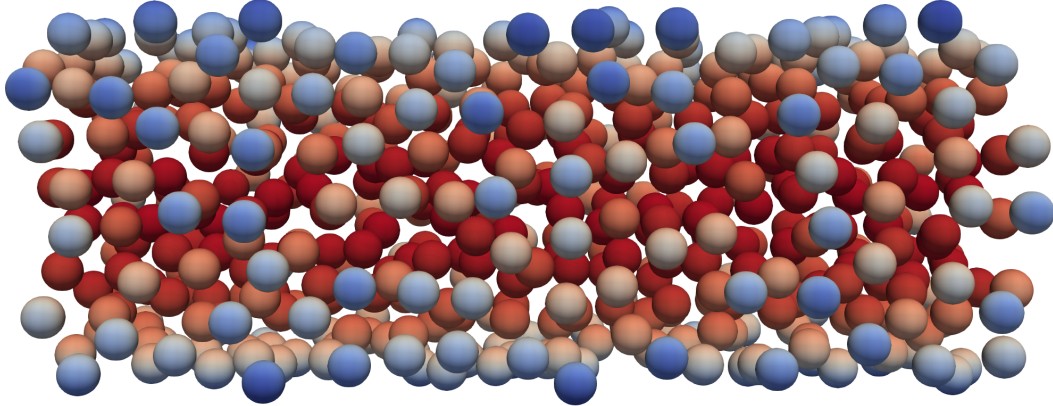


Figure 14: Instantaneous snapshot from a simulation with $N = 500$ capsules in duct flow. The flow is from left to right with the color indicating the velocity magnitude of the capsule membrane.

relatively coarse grid of $200 \times 500 \times 200$ and a fixed time step of $5e-5$ for all simulations. The Reynolds number, based on the mean flow velocity and channel width, is set to 0.2, and the capillary number $Ca = 0.5$. Figure 14 shows the instantaneous configuration of the capsules for $N=500$.

We examine how the computational time per iteration varies with the number of capsules N . All simulations are performed using 128 processors and are run for 1000 time steps. We look at the mean wall-clock time per time step, averaged over all processors and time steps. Each computational step of this analysis follows the algorithm outlined in Figure 4, with the exception of the extrapolation and diffusion steps, which are excluded from the measurements. Table 2 summarizes the results for increasing values of N , starting from a baseline case with a single capsule. As it can be read in the table, the increase in computational cost remains minimal even for the case with $N = 500$, which corresponds to approximately 10.5% volume fraction of capsules in the domain.

N	Time (sec)
1	0.667
10	0.675
50	0.695
100	0.721
200	0.752
500	0.812

Table 2: Computational time per time step for an increasing number of capsules, N in duct flow, see visualisation in figure 14.

5 Conclusions

We present a fully-Eulerian diffuse-interface framework to simulate capsules and elastic membrane in fluid flow for a variety of configurations. The capsule consists of a fluid enclosed by a thin elastic membrane, moving and deforming in a second fluid, with both fluids assumed as Newtonian in the present case.

A conservative diffuse-interface method is adopted to track the membrane, i.e. the elastic interface between inner and outer fluids. The elastic stresses on the membrane are obtained from an energy functional of the local strain, which is obtained from the gradient of the reference map linking the reference and present configurations. We propose here a modified advection equation for the reference map which ensures a consistent transport of the strain tensor and of the interface location. The additional term of the reference-map transport equation is obtained by minimizing the error functional that quantifies the discrepancy between the interface location as defined by the reference map itself and by the phase field. The accuracy of the method is demonstrated here by a series of validation cases of increasing complexity.

We also introduce an efficient tagging procedure, based on the reference map to the initial configuration, that greatly reduces the computational cost of multi-capsule setups. The tagging allows to compute the deformation and stresses on each capsule, and potentially consider capsule-capsule short-range interaction forces, e.g. repulsion and attraction. We show here that the proposed approach enables the simulations of hundreds of capsules without significant additional computational cost relative to the single-capsule cases.

The Eulerian method proposed here is highly scalable and well-suited for large-scale parallel simulations and can easily be implemented in existing two-phase solvers with minimal effort. Moreover, the framework provides a robust platform for studying coupled transport phenomena, such as mixing and gas transfer in cell suspensions, exploiting existing accurate and efficient implementations of scalar transport and interfacial fluxes within the the diffuse interface frameowrk [26, 27, 28].

References

- [1] S Ramanujan and C Pozrikidis. Deformation of liquid capsules enclosed by elastic membranes in simple shear flow: large deformations and the effect of fluid viscosities. *Journal of fluid mechanics*, 361:117–143, 1998.
- [2] Sai K Doddi and Prosenjit Bagchi. Lateral migration of a capsule in a plane poiseuille flow in a channel. *International Journal of Multiphase Flow*, 34(10):966–986, 2008.
- [3] Xiaoyi Li and Kausik Sarkar. Front tracking simulation of deformation and buckling instability of a liquid capsule enclosed by an elastic membrane. *Journal of Computational Physics*, 227(10):4998–5018, 2008.

- [4] Hong Zhao, Amir HG Isfahani, Luke N Olson, and Jonathan B Freund. A spectral boundary integral method for flowing blood cells. *Journal of Computational Physics*, 229(10):3726–3744, 2010.
- [5] Dmitry A Fedosov, Bruce Caswell, and George Em Karniadakis. A multiscale red blood cell model with accurate mechanics, rheology, and dynamics. *Biophysical journal*, 98(10):2215–2225, 2010.
- [6] Constantine Pozrikidis. *Computational hydrodynamics of capsules and biological cells*. CRC press, 2010.
- [7] Thomas Milcent and Emmanuel Maitre. Eulerian model of immersed elastic surfaces with full membrane elasticity. In *IW on numerical methods and applications in fluid-structure interactions*, page 28, 2014.
- [8] Georges-Henri Cottet, Emmanuel Maitre, and Thomas Milcent. *Level set methods for fluid-structure interaction*. Springer, 2022.
- [9] Florian Desmons, Thomas Milcent, Anne-Virginie Salsac, and Mirco Ciallella. Fully eulerian models for the numerical simulation of capsules with an elastic bulk nucleus. *Journal of Fluids and Structures*, 127:104109, 2024.
- [10] Maximilian Kloppe and Sebastian Aland. A phase-field model of elastic and viscoelastic surfaces in fluids. *Computer Methods in Applied Mechanics and Engineering*, 428:117090, 2024.
- [11] Pao-Hsiung Chiu and Yan-Ting Lin. A conservative phase field method for solving incompressible two-phase flows. *Journal of Computational Physics*, 230(1):185–204, 2011.
- [12] Suhas S Jain. Accurate conservative phase-field method for simulation of two-phase flows. *Journal of Computational Physics*, 469:111529, 2022.
- [13] Shahab Mirjalili, Suhas S Jain, and Micheal Dodd. Interface-capturing methods for two-phase flows: An overview and recent developments. *Center for Turbulence Research Annual Research Briefs*, 2017(117-135):13, 2017.
- [14] Shahab Mirjalili, Christopher B Ivey, and Ali Mani. A conservative diffuse interface method for two-phase flows with provable boundedness properties. *Journal of Computational Physics*, 401:109006, 2020.
- [15] Marco Crialesi-Esposito, Nicolò Scapin, Andreas D Demou, Marco Edoardo Rosti, Pedro Costa, Filippo Spiga, and Luca Brandt. Flutas: A gpu-accelerated finite difference code for multiphase flows. *Computer Physics Communications*, 284:108602, 2023.

- [16] Boris Valkov, Chris H Rycroft, and Ken Kamrin. Eulerian method for multiphase interactions of soft solid bodies in fluids. *Journal of Applied Mechanics*, 82(4):041011, 2015.
- [17] Chunming Li, Chenyang Xu, Changfeng Gui, and Martin D Fox. Level set evolution without re-initialization: a new variational formulation. In *2005 IEEE computer society conference on computer vision and pattern recognition (CVPR'05)*, volume 1, pages 430–436. IEEE, 2005.
- [18] Ken Kamrin, Chris H Rycroft, and Jean-Christophe Nave. Reference map technique for finite-strain elasticity and fluid–solid interaction. *Journal of the Mechanics and Physics of Solids*, 60(11):1952–1969, 2012.
- [19] Chris H Rycroft, Chen-Hung Wu, Yue Yu, and Ken Kamrin. Reference map technique for incompressible fluid–structure interaction. *Journal of Fluid Mechanics*, 898:A9, 2020.
- [20] Matthias Teschner, Stefan Kimmerle, Bruno Heidelberger, Gabriel Zachmann, Laks Raghupathi, Arnulph Fuhrmann, M-P Cani, François Faure, Nadia Magnenat-Thalmann, Wolfgang Strasser, et al. Collision detection for deformable objects. In *Computer graphics forum*, volume 24, pages 61–81. Wiley Online Library, 2005.
- [21] Shiguang Liu, Qiguang Liu, and Qunsheng Peng. Realistic simulation of mixing fluids. *The Visual Computer*, 27:241–248, 2011.
- [22] Pedro Costa. A fft-based finite-difference solver for massively-parallel direct numerical simulations of turbulent flows. *Computers & Mathematics with Applications*, 76(8):1853–1862, 2018.
- [23] Rafael Diez Sanhueza, Jurriaan Peeters, and Pedro Costa. A pencil-distributed finite-difference solver for extreme-scale calculations of turbulent wall flows at high reynolds number. *arXiv preprint arXiv:2502.06296*, 2025.
- [24] X-Q Hu, A-V Salsac, and D Barthès-Biesel. Flow of a spherical capsule in a pore with circular or square cross-section. *Journal of Fluid Mechanics*, 705:176–194, 2012.
- [25] Rajesh Kumar Singh and Kausik Sarkar. Hydrodynamic interactions between pairs of capsules and drops in a simple shear: Effects of viscosity ratio and heterogeneous collision. *Physical Review E*, 92(6):063029, 2015.
- [26] Suhas S Jain. A model for transport of interface-confined scalars and insoluble surfactants in two-phase flows. *Journal of Computational Physics*, 515:113277, 2024.
- [27] Shahab Mirjalili, Suhas S Jain, and Ali Mani. A computational model for interfacial heat and mass transfer in two-phase flows using a phase field method. *International Journal of Heat and Mass Transfer*, 197:123326, 2022.

- [28] Salar Zamani Salimi, Andrea Gruber, Nicolò Scapin, and Luca Brandt. Evaporation of finite-size ammonia and n-heptane droplets in weakly compressible turbulence: An interface-resolved dns study. *arXiv preprint arXiv:2504.16850*, 2025.